



## Capability of the penetrator seismometer system for lunar seismic event observation

R. Yamada<sup>a,b,\*</sup>, I. Yamada<sup>c</sup>, H. Shiraishi<sup>a</sup>, S. Tanaka<sup>a</sup>, Y. Takagi<sup>d</sup>, N. Kobayashi<sup>e</sup>, N. Takeuchi<sup>f</sup>, Y. Ishihara<sup>g</sup>, H. Murakami<sup>h</sup>, K. Yomogida<sup>i</sup>, J. Koyama<sup>i</sup>, A. Fujimura<sup>a</sup>, H. Mizutani<sup>a,j</sup>

<sup>a</sup> Institute of Space and Astronautical Science, Japan Aerospace Exploration Agency, 3-1-1 Yoshinodai, Sagami-hara, Kanagawa 229-8510, Japan

<sup>b</sup> Department of Earth and Planetary Science, University of Tokyo, Bunkyo-ku, Tokyo 113-0033, Japan

<sup>c</sup> Research Center for Seismology, Volcanology and Disaster Mitigation, Nagoya University, Chikusa-ku, Nagoya, Aichi 464-8602, Japan

<sup>d</sup> Mitutoyo Corporation, Kawasaki, Kanagawa 213-8533, Japan

<sup>e</sup> Department of Earth and Planetary Science, Tokyo Institute of Technology, Meguro-ku, Tokyo 152-8551, Japan

<sup>f</sup> Earthquake Research Institute, University of Tokyo, Bunkyo-ku, Tokyo 113-0032, Japan

<sup>g</sup> Japan Agency for Marine-Earth Science and Technology, Yokohama, Kanagawa 236-0001, Japan

<sup>h</sup> Department of Applied Science, Faculty of Science, Kochi University, Kochi 780-8520, Japan

<sup>i</sup> Department of Earth and Planetary Science, Hokkaido University, Sapporo, Hokkaido 060-0810, Japan

<sup>j</sup> Newton Press Inc, Shinjuku-ku, Tokyo 163-0207, Japan

### ARTICLE INFO

#### Article history:

Received 28 March 2008

Received in revised form

28 November 2008

Accepted 1 December 2008

Available online 13 December 2008

#### Keywords:

Seismometer

Penetrator

Moonquake

Lunar exploration

Planetary seismology

### ABSTRACT

We developed a seismometer system for a hard landing “penetrator” probe in the course of the former Japanese LUNAR-A project to deploy new seismic stations on the Moon. The penetrator seismometer system (PSS) consists of two short-period sensor components, a two-axis gimbal mechanism for orientation, and measurement electronics. To carry out seismic observations on the Moon using the penetrator, the seismometer system has to function properly in a lunar environment after a hard landing (impact acceleration of about 8000G), and requires a signal-to-noise ratio to detect lunar seismic events. We evaluated whether the PSS could satisfactorily observe seismic events on the Moon by investigating the frequency response, noise level, and response to ground motion of our instrument in a simulated lunar environment after a simulated impact test. Our results indicate that the newly developed seismometer system can function properly after impact and is sensitive enough to detect seismic events on the Moon. Using this PSS, new seismic data from the Moon can be obtained during future lunar missions.

© 2008 Elsevier Ltd. All rights reserved.

### 1. Introduction

During the Apollo lunar landing missions (1969–1972), a passive seismic network consisting of four stations (Apollo 12, 14, 15, and 16) was constructed on the nearside of the Moon to investigate lunar seismicity. The network observation continued until 1977, and provided us with information about several types of seismic events (deep moonquakes, shallow moonquakes, thermal moonquakes, and meteoroid impacts) and their unique characteristics, as well as the internal structure of the Moon (Latham et al., 1973; Toksöz et al., 1974; Lammlin, 1977; Goins et al., 1979; Nakamura et al., 1982; Khan and Mosegaard, 2002; Lognonné et al., 2003; Gagnepain-Beyneix et al., 2006). However,

we still need a better understanding of the physical mechanisms of moonquakes and the structure and composition of the deep interior of the Moon, since the Apollo data were limited by the small number of stations and their regional locations on the nearside. We require more lunar seismic data from a global seismic network to obtain further information about the whole interior of the Moon, especially the core.

We developed a hard landing “penetrator” probe in the course of the former Japanese LUNAR-A project (Mizutani et al., 2000, 2003) to deploy new seismic stations on the Moon. The cross-sectional diagram of the LUNAR-A penetrator is shown in Fig. 1. The penetrator was designed to be deployed into the lunar regolith at a depth of 1–3 m by free fall from a spacecraft orbiting around the Moon. Hence instruments in the penetrator need to be able to survive the high-speed impact (impact acceleration of about 8000G) (Mizutani et al., 1999). The penetrator has notable advantages over other types of probes (installed by a soft-lander or by astronauts) in constructing a global geophysical network on the Moon. The principal advantage of the penetrator is that

\* Corresponding author at: Institute of Space and Astronautical Science, Japan Aerospace Exploration Agency, Room 1558A, 3-1-1 Yoshinodai, Sagami-hara, Kanagawa 229-8510, Japan. Tel.: +81042 7598200; fax: +81042 7598516.

E-mail address: [ryamada@planeta.sci.isas.jaxa.jp](mailto:ryamada@planeta.sci.isas.jaxa.jp) (R. Yamada).

multiple stations can be deployed in one flight because the penetrator is smaller and lighter than conventional soft-landers, so a spacecraft can potentially carry a multiple number of probes in a limited weight budget. It is also of lower cost than a human deployment. In addition, the penetrator is placed in a more stable temperature environment compared with deployment on the lunar surface, due to the thermal insulation of the lunar regolith. Lastly, the penetrator's good contact with the regolith provides an ideal environment for seismic observations.

To take advantage of these attributes, we developed a compact seismic sensor for the penetrator. The sensor is combined with the gimbal mechanism for attitude control after penetration, and measurement electronics for recording seismic data in the penetrator. We have already confirmed that the sensor itself has shock durability and works as designed even after an impact penetration (Yamada et al., 2005; Shiraishi et al., 2008). However, we must confirm that the entire penetrator seismometer system (PSS) consisting of the sensors, the gimbal mechanism, and the electronics assembled into the penetrator functions properly and has the signal-to-noise ratio required to detect seismic events in a lunar environment after a hard landing with an impact acceleration of about 8000 G.

In this paper, we describe the current specifications of the PSS—the frequency response, response to ground motion, and noise level—before penetrating into the lunar surface (Section 2). Then, we describe the effects of the lunar temperature and gravity environment (Section 3), and those of the penetrating impact (Section 4) on these specifications. Finally, we discuss whether the PSS developed by our team can satisfactorily detect seismic events

on the Moon against the combined effects of the impact and the lunar environment (Section 5).

## 2. Performance of the PSS before impact

The PSS consists of two sensor components: one horizontal and one vertical, along with a two-axis gimbal mechanism (for orientation) and measurement electronics (amplifiers, filters, A/D converter, and memory). In this section, we describe the current instrument specifications: the frequency response, response to ground motion, and noise level of PSS before penetrating into the lunar surface.

### 2.1. Frequency response

From previous analysis of three types of lunar seismic events (deep moonquakes, shallow moonquakes, and meteoroid impacts) detected by the Apollo seismometers, it is known that shallow moonquakes and meteoroid impacts typically have higher frequency content and larger amplitudes than deep moonquakes. Many deep moonquakes were detected by the Apollo long-period (LP) seismometer in peaked response mode (Latham et al., 1973), with little energy in the short-period component (Dainty et al., 1975). Some researchers estimated that the dominant frequency of deep moonquakes was about 1 Hz (Lammlein et al., 1974; Goins et al., 1981; Araki, 1994). If the PSS has a better frequency response than those of the Apollo seismometers at 1 Hz and higher, it should be able to detect both deep moonquakes and other higher frequency content seismic events.

The frequency response of the PSS is represented by those of both the sensor and the measurement electronics. The frequency response  $T(\omega)$  of the sensor is represented by

$$T(\omega) = G_C \omega^2 / (\omega_0^2 - \omega^2 - i2\omega\omega_0 h),$$

$$\omega_0 = 2\pi f_0, \quad (1)$$

where  $\omega$  is angular frequency in radian,  $\omega_0$  is resonant angular frequency in radian,  $f_0$  is resonant frequency in Hz,  $h$  is damping constant and  $G_C$  is generator constant in V/m/s (Havskov and Alguacil, 2004). The sensor for the penetrator is a short-period electromagnetic seismic sensor with velocity output, consisting of signal coils as a pendulum suspended by a pair of diaphragm springs, and magnetic circuits fixed to the reference frame (Fig. 2).

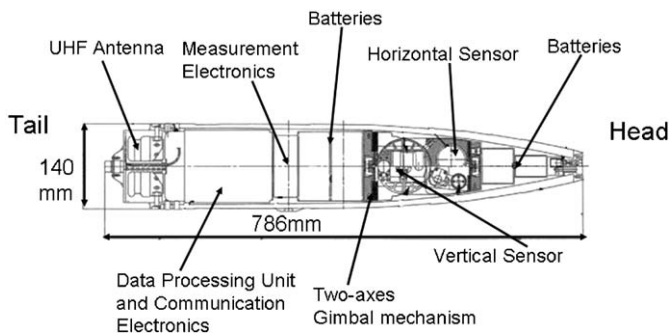


Fig. 1. The cross-sectional diagram of the penetrator. The view is from the lateral.

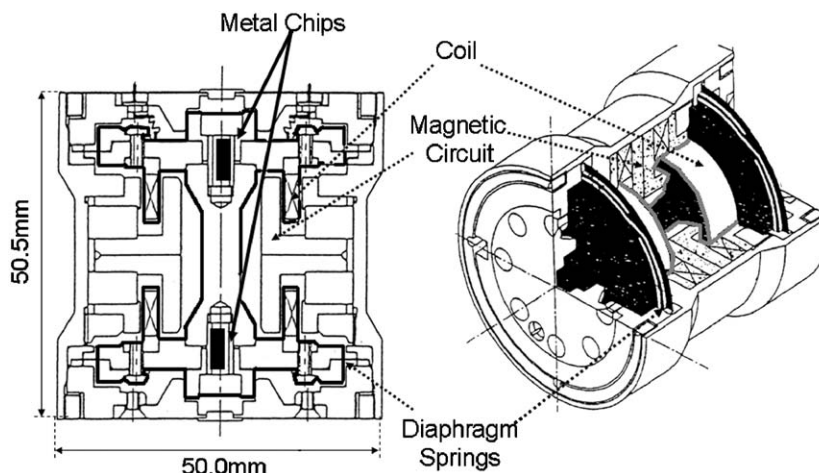
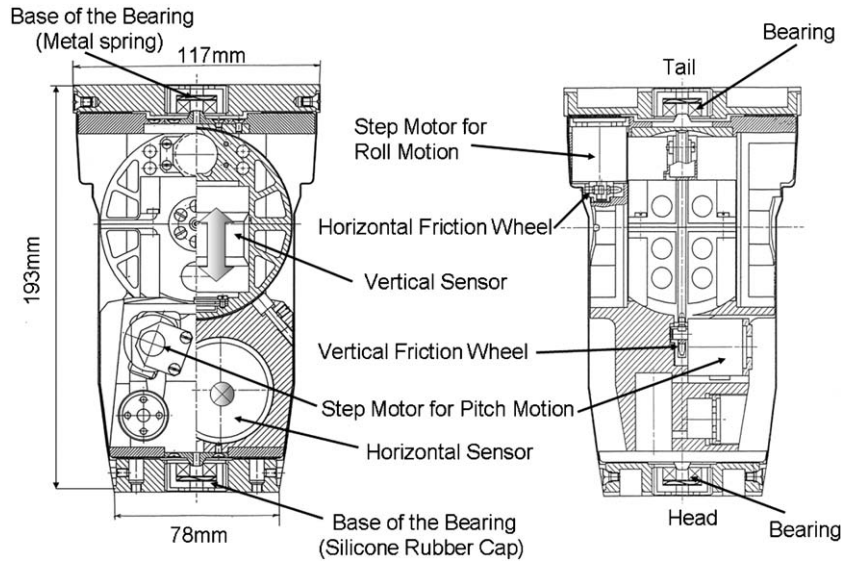


Fig. 2. The cross-sectional diagram and bird-eye view of the sensor for the penetrator. The pendulum of the sensor is surrounded by the bold solid line in the cross-sectional diagram.



**Fig. 3.** Cross-sectional diagrams of the sensors as assembled into the gimbal mechanism. The left view is from the lateral and the right view is from the front. The terms 'Tail' and 'Head' in the right view indicates the directions of the gimbal mechanism in the penetrator (Fig. 1). Two sensor components are supported by a pair of friction wheels (vertical and horizontal) and two opposite bearings. The arrow mark on the vertical sensor and cross mark on the horizontal sensor in the lateral view represent the directions of the sensitive axes of the vertical and horizontal sensors, respectively. A silicone rubber cap and a metal spring are used on the base of the bearings to absorb penetrating shocks. The attitudes of the sensors are adjusted by the friction wheels, which are attached with two-axis motors.

When the suspended signal coil (pendulum) is oscillated by the ground motion, the voltage output arises in proportion to the velocity of the pendulum relative to the fixed magnet. Because of a mass budget and an electrical power limitation (760 Wh) in the penetrator, a passive and very compact sensor is applied.

The very compact size and lightweight nature of the passive sensor have made its resonant frequency higher than the desired 1 Hz (about 2–3 Hz). Then, we have made two improvements to achieve a better frequency response for moonquake observation. The first improvement was made to lower the resonant frequency of the sensor. The critical factor contributing to the resonant frequency of the sensor is the spring constant of the diaphragm spring, which is usually controlled by its mechanical response. It initially appears difficult to lower the resonant frequency of the sensor without changing the physical size of the spring.

Therefore, small metal chips attached at both ends of the pendulum of the sensor can be used to cancel the mechanical restoring force of the spring with a magnetic force (Fig. 2). By selecting appropriate sizes and positions of the metal chips, we can lower the resonant frequency without a significant mass increase. The second improvement made to the sensor was heightening the total gain. The total gain of the PSS is calculated by combining the generator constant of the sensor and the amplifier gain in the electronics. The generator constant  $G_C$  is expressed as

$$G_C = 2\pi aNB, \quad (2)$$

where  $a$  is radius of the coil in meter,  $N$  is number of turns of the coil,  $B$  is magnetic flux density in the magnetic circuit in Tesla. From Eq. (2), it is found that more number of turns of the coil and stronger magnetic flux cause larger generator constant. In case of our sensor, magnetic circuits that have a strong magnetic flux density (0.6–0.7 T at maximum) and coils with many turns are installed to heighten the generator constant. The generator constant is over 1000 V/m/s. In addition, high-gain amplifiers (6000 times) are installed in the electronics. From the improvements, the total gain factor of about  $6.3E+6$  V/m/s is achieved.

The use of small metal chips and magnetic circuits that have a strong magnetic field to achieve better frequency response raised concerns about magnetic interference between the two sensor components once assembled into the gimbal mechanism, since the vertical and horizontal sensors are set only about 2 cm from one another (Fig. 3). The strong magnetic field leaking from the magnetic circuit of one sensor may influence the metal chips and the magnetic circuit of the other, affecting sensor performance. To account for this effect, we wound a carbon steel magnetic shield plate around the horizontal sensor to reduce the influence of its magnetic interference, and investigated the frequency responses of the two sensors before and after assembling into the PSS.

The frequency response (resonant frequencies, damping constants, and generator constants) of the sensors were determined from fitting the dynamic equation of the mass-spring system to the calibration pulses using least square method (e.g., Havskov and Alguacil, 2004). In our sensor, a test coil is wound around the signal coil on the pendulum for calibration. A calibration pulse is generated by applying a step current to the test coil. We obtained many calibration pulses from two-component sensors before and after assembling into the gimbal mechanism and connecting into the measurement electronics. We stacked the waveforms of the calibration pulses to enhance the signal-to-noise ratio. From analysis of the stack, it was found that the frequency responses did not change due to magnetic interference within measurement deviation after assembling the sensors into the gimbal mechanism.

From these results, we find that the PSS can achieve a higher gain in the higher frequency range over 1 Hz than those of the Apollo seismometers (Fig. 4). The specifications of the PSS and Apollo LP seismometer system are compared in Table 1.

## 2.2. Response to ground motion

We now describe the response of the sensor and the gimbal mechanism to actual ground motion. In the gimbal mechanism, a pair of friction wheels and two opposing bearings support the

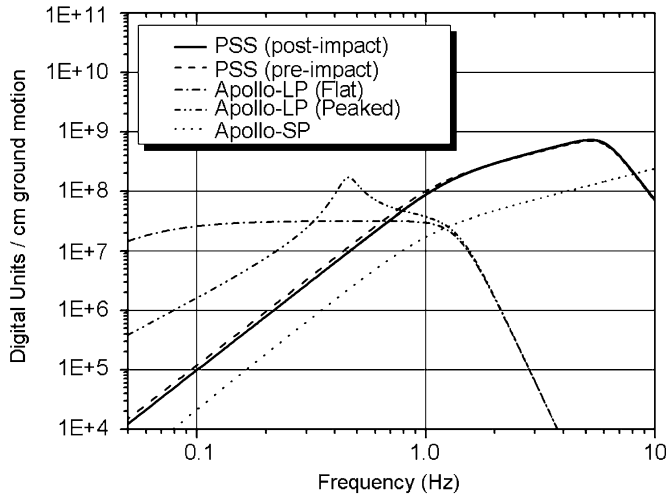


**Fig. 4.** The frequency response curves of the PSS (pre-impact and post-impact (horizontal)) and Apollo seismometers. ‘LP’ is an abbreviation for long-period. ‘SP’ is an abbreviation for short-period. The frequency response curve of the post-impact PSS is assumed to be achieved in the lunar regolith near the lunar equator. On the frequency response curve of the PSS, the filter which has bandwidth of 0.01–6.0 Hz in the measurement electronics causes the down slope in higher frequency range over 6.0 Hz.

**Table 1**  
Comparison between the penetrator seismometer system and Apollo long-period seismometer (Latham et al., 1970; Horvath, 1979)

	PSS	Apollo LP
Sensor type	Electro magnetic sensor	Capacitive displacement sensor
Component	Horizontal:one Vertical:one	Horizontal:two Vertical:one
Resonant frequency	1.1 (Hz)	0.067 (Hz)
Damping constant	0.65	0.85
Total gain	6.3E+6 (V/m/s)	15E+6 (V/m)
Assembled size	Height 19 cm × diameter 12 cm (in gimbal mechanism)	Height 29 cm × diameter 23 cm
Assembled mass	2.1 (kg) (in gimbal mechanism)	11.5 (kg)
Frequency range	0.01–6.00 (Hz)	0.0004–2.00 (Hz)
Sampling rate	16 (Hz)	6.62 (Hz)
Resolution	10 (bit)	10 (bit)

sensors (Fig. 3). The wheels are made of silicon rubber to sustain the sensors by frictional force, and a silicone rubber cap and a metal spring are put on the base of the bearings to absorb shock. Each friction wheel (vertical and horizontal) is attached with a pair of step motors in the gimbal mechanism (Fig. 3). When the pulse currents are applied to the motor, it rotates the friction wheel dependent on number of the pulses. The orientation of the sensor can be adjusted by rotating the friction wheel. The elasticity of silicone rubber affects the coupling condition of the sensors with the penetrator body which may make a difference in waveforms observed by the sensors inside the gimbal mechanism. Although our test has already confirmed that the sensor assembled into the gimbal mechanism has the proper response to step currents (calibration pulses) before a penetrating impact as described in upper section, the response of the assembled sensor after the penetration to actual ground motion (microtremor) is described in Section 4.2.

### 2.3. Noise level

For estimation of the signal-to-noise ratio for lunar seismic events, we have to evaluate the noise level of the PSS. The noise component of the PSS consists of Johnson noise (thermal noise), suspension noise (Brownian noise), and voltage and current noises.

A seismic sensor produces Johnson noise and suspension noise. Johnson noise is the random voltage produced across a resistance by the thermal agitation of electronics, and suspension noise arises from Brownian motion of the gas molecules around the pendulum. The voltage power spectral density (PSD) of Johnson noise ( $J_n$ ) is represented as

$$J_n = 4kTR_C, \quad (3)$$

where  $J_n$  is measured in  $V^2/\text{Hz}$ ,  $k$  is the Boltzmann constant ( $1.38 \times 10^{-23} \text{ J/K}$ ),  $T$  is temperature in K, and  $R_C$  is coil resistance in ohms (Rodgers, 1992). The acceleration PSD of suspension noise ( $S_n$ ) is expressed as

$$S_n = 16\pi kThf_0/M, \quad (4)$$

where  $S_n$  is measured in  $(\text{m/s}^2)^2/\text{Hz}$ ,  $f_0$  is the resonant frequency of the spring-mass system in Hz,  $h$  is the damping constant of the spring-mass system, and  $M$  is the mass of the pendulum in kg (Aki and Richards, 2002). The acceleration PSD is converted to voltage PSD ( $P_S$ ) by the frequency response function of the seismometer system for acceleration

$$P_S = |H(\omega)|^2 * G_C^2 * S_n, \quad (5)$$

where  $H(\omega)$  is the frequency response function of the seismometer system with velocity output for ground acceleration in  $1/s$ .

Three types of noise components (Johnson noise, voltage noise, and current noise) are considered as the noise of the pre-amplifier (Rodgers, 1992). In the PSS, an OP-97 operational amplifier is used as the pre-amplifier. Based on the manufacturer's sheet data on OP-97, we construct the PSD models for the voltage and current noises. The total electrical noise ( $E_n$ ) appearing at the input stage of the pre-amplifier is given by the following equation:

$$E_n = V_n + I_n R_C^2 + J_{en}, \quad (6)$$

where  $V_n$  is the PSD of voltage noise in  $V^2/\text{Hz}$ ,  $I_n$  is the PSD of current noise in  $A^2/\text{Hz}$ , and  $J_{en}$  is the PSD of Johnson noise from the pre-amplifier circuit in  $V^2/\text{Hz}$ .

Then the PSD of the total voltage noise ( $P_{nn}$ ) at the input stage of the pre-amplifier is obtained by summing the total electrical noise  $E_n$ , the suspension noise  $P_S$ , and Johnson noise  $J_n$

$$P_{nn} = E_n + P_S + J_n, \quad (7)$$

where  $P_{nn}$  is measured in  $V^2/\text{Hz}$ . This input voltage noise  $P_{nn}$  passes through the electrical circuits of the PSS, and it is amplified and filtered by the components in the circuit. Through the passage of the circuit, the Johnson noise and electrical noise are added to the voltage noise ( $P_{nn}$ ), and the total output noise is obtained. The input equivalent noise is obtained by dividing the voltage PSD of the total output noise by the resultant amplifier gain. The calculated voltage PSD of the input equivalent noise is plotted in Fig. 5. The noise model was confirmed by direct measurement of the output noise. We measured the output noise of the PSS without suspension noise by preventing the pendulum from moving. Since the suspension noise is caused from the oscillation of the pendulum by the Brownian motion of the gas molecules around the pendulum, it arises with the seismic signal. Although lighter pendulum's mass of the sensor generates larger suspension noise as expressed in Eq. (4), it is still smaller than seismic signal in the laboratory. For this reason, it is very difficult to measure the suspension noise away from the seismic signal. The comparison of

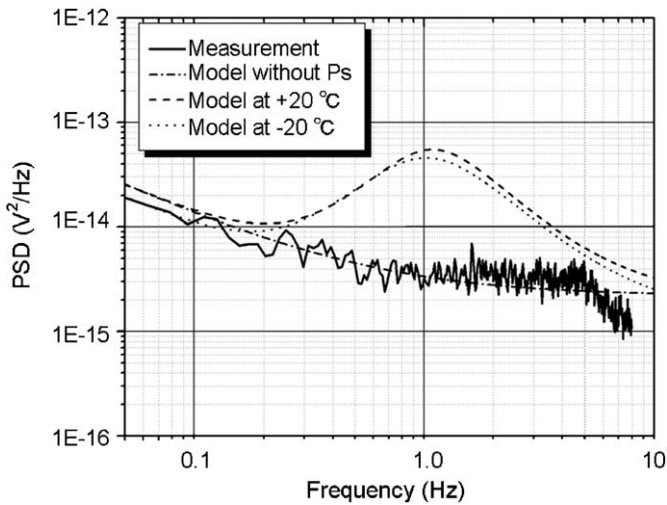


**Fig. 5.** The voltage PSD profiles of input equivalent noise at the input stage of the pre-amplifier of the PSS. The bold solid line indicates the PSD of the measured noise, and the chained line indicates the PSD of the calculated input equivalent noise without suspension noise ( $P_s$ ). The dashed line and the dotted line indicate the noise PSD including the suspension noise at +20 and  $-20^\circ\text{C}$ , respectively.

the measured data with the noise model without the suspension noise ( $P_s$ ) indicates that the model can represent the measured noise of the PSS (Fig. 5). In actual seismic observation on the Moon, the suspension noise exists in the output noise because dry xenon gas is used to fill in the gimbal mechanism, to lubricate its movement. We use the noise model with the suspension noise to estimate the signal-to-noise ratio of our seismometer system.

### 3. Effects of the lunar environment

The temperature at the predicted penetration depth of about 2 m in the regolith near the lunar equator is approximately  $-20^\circ\text{C}$  and is almost constant (Langseth and Keihm, 1977), and the lunar gravity is one-sixth of the Earth's gravity. The effects of low temperature and low gravity can change the frequency response, response to ground motion, and the noise level of the PSS. In this section, we describe these lunar environmental effects on the performance of the PSS.

#### 3.1. Effect on the frequency response

The frequency response (resonant frequency, damping constant, and generator constant) of the sensor changes due to a decrease in temperature. We obtained some calibration pulses from two sensor components set in a thermal chamber whose internal temperature varied from +20 (room temperature) to  $-20^\circ\text{C}$ . From analysis of these pulses, the change of the frequency responses of the sensors with temperature was derived.

Fig. 6(a) shows the temperature dependences of the resonant frequencies of the horizontal and the vertical sensors. The results indicate that a decrease in temperature makes the resonant frequency decrease linearly with slopes of about  $4.0\text{E-}3\text{ Hz per degree}$  for the horizontal and  $1.4\text{E-}3\text{ Hz per degree}$  for the vertical. Fig. 6(b) shows the linear relationship between the damping constant and temperature. In this case, the slopes are about  $-2.4\text{E-}3$  per degree for the horizontal and about  $-1.2\text{E-}3$  per degree for the vertical. For the generator constant, it was found that the values for both horizontal and vertical increased by about 1.5% with a decrease in temperature of  $40^\circ\text{C}$ .

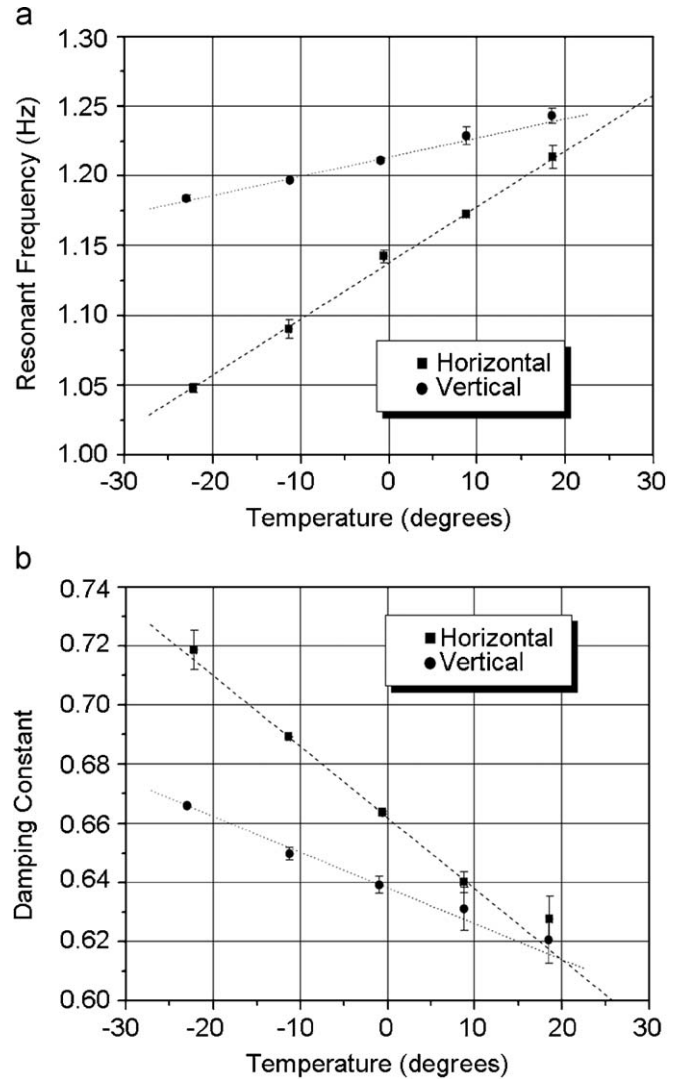


**Fig. 6.** (a) The measured resonant frequencies and (b) the measured damping constants of the horizontal and vertical sensors at some temperatures in thermal range from +20 to  $-20^\circ\text{C}$ .

The results showed that the change in the frequency response of the vertical sensor with temperature was smaller than that of the horizontal sensor. The vertical sensor uses a pair of diaphragm springs which has different nature compared to that of the horizontal sensor to sustain the pendulum against the lunar gravitational force. Its difference may cause the different temperature characteristics. The differences of size and positions of metal chips inserted into the pendulum of the horizontal and the vertical sensors may also cause the different temperature characteristics. We use these correction coefficients for temperature to estimate the frequency responses of two sensor components at low temperature.

We were concerned about the magnetic interference between the two sensor components under different temperatures, because the leaking magnetic field from the magnet circuit changes with temperature. We measured the flux density of the leaking magnetic field from  $-20$  to  $+20^\circ\text{C}$ , and the results showed an increase in magnetic flux density of about 8%. However, the magnetic permeability of the carbon steel magnetic shield plate hardly changes in this temperature range (Chikazumi, 1981). Thus, we conclude that the shield plate can negate the small increase in

magnetic flux under the low temperatures present in the lunar regolith.

Although the lunar gravity will not change the frequency response of the sensor, it changes the angle where the vertical sensor pendulum is set at neutral position. The neutral position of the vertical sensor is designed to be met almost  $0^\circ$  from the vertical (i.e., the gravitational direction) under the lunar gravity. To equate the effects of Earth's and lunar gravity, we use

$$g_m = g_e \cos \theta_v, \quad (8)$$

where  $g_e$  and  $g_m$  are the Earth's and lunar gravitational acceleration in  $m/s^2$ , respectively, and  $\theta_v$  is the inclination of the vertical sensor from the vertical in degrees. From Eq. (8), the vertical sensor pendulum is set at neutral position at about  $80^\circ$  from the vertical (or  $10^\circ$  from the horizontal) under the Earth's gravity.

Next, we investigated the response of the measurement electronics to an input signal under different temperatures. We placed the measurement electronics of the PSS in a thermal chamber and input sinusoidal waves at 1 Hz using a signal generator. The outputs through the electronics were measured at  $+20$  and  $-20^\circ\text{C}$ , and it was found that the amplitudes and wavelengths of the output waveforms did not change in this temperature range. We conclude that the response of the measurement electronics to signal waves at a frequency of about 1 Hz can be preserved in the lunar temperature environment.

### 3.2. Effects on response to ground motion

As described in Section 2.2, the elastic contacts between the sensor and the silicone components (the friction wheel and the base of the bearings) can affect the response to ground motion. Since the lunar surface temperature and lunar gravity can change the contact conditions, we estimated how the conditions vary with the environment.

We represented the elastic contact condition (coupling condition of the sensors with the penetrator body) by the spring constants of the silicone components. To evaluate the spring constants, the shrinkage of the silicone components was measured under a vertical load. In this measurements, the actual contact conditions between the silicone components and the gimbal mechanism were simulated. The friction wheel was pressed vertically by a mass block and the vertical load and the shrinkage of the friction wheel were measured. From the measurement, it was found that the friction wheel was deformed non-linearly in the axial direction under an increased vertical load. Fig. 7 shows the measured relationship between the vertical load and the shrinkage of the friction wheel at  $+20$  and  $-20^\circ\text{C}$ . Because the friction wheel deforms non-linearly with load, the spring constant of the friction wheel changes. Since the load of the gimbal mechanism on the friction wheel depends on the gravity as well as the inclination of the penetrator, the spring constants of the wheels change with the gravity and inclination of the penetrator in addition to temperature.

In the measurement of the spring constant of the bearing base, the mass block whose edges (contact surface) were similar to those of gimbal mechanism was pushed on the bearings. The relations between shrinkage of the bearing base and the vertical load were measured in radial and axial directions. The measurements showed that the base of bearings linearly shrank, and that the shrinkage of the base of bearings in radial direction was much smaller than that in axial direction. We can say that the base of bearings shrinks to only axial direction. The linear shrinkage indicates that the spring constant of the base of bearings does not change depending on the gravity and the inclination of the penetrator, but it will change with temperature.

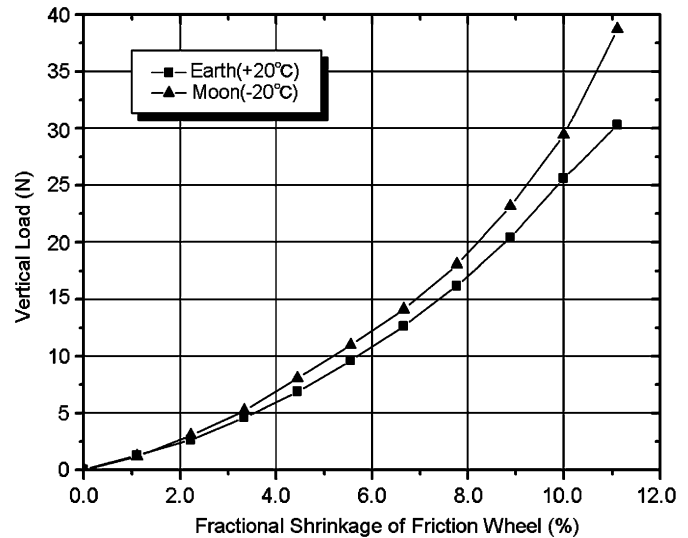


Fig. 7. The measured relationship between the vertical load and the shrinkage of the friction wheel at  $+20$  and  $-20^\circ\text{C}$ . The horizontal axis is expressed as fractional shrinkage (%) for the friction wheel which has diameter of 18 (mm). The temperature of  $+20^\circ\text{C}$  is the room temperature; it is assumed to be a typical value on the Earth. The temperature of  $-20^\circ\text{C}$  is considered to be typical in the lunar regolith near the equator.

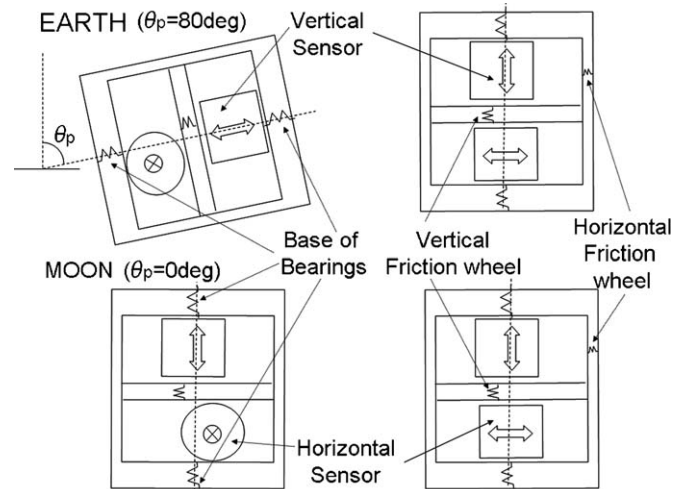
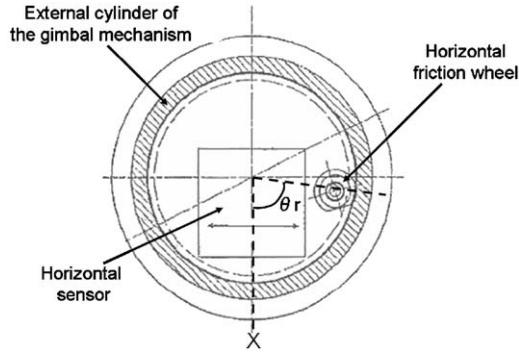


Fig. 8. Schematic diagram of two sensor components sustained by the silicone components such as friction wheel and base of the bearings in the gimbal mechanism under the Earth's and lunar gravity. The two component sensors are set at neutral positions, and the silicone components are expressed as springs by analogy. The left view is from the lateral and the right view is from the front as shown in Fig. 3.  $\theta_p$  indicates the inclination of the gimbal mechanism and the penetrator from the vertical. The dashed line in the gimbal mechanism is its center axis, and it coincides with the longitudinal axis of the penetrator. The gimbal mechanism is inclined at  $80^\circ$  under the Earth's gravity, and it is set at the vertical under the lunar gravity. The cross mark and the bold arrow mark on the sensors indicate each sensitive axis of two sensors.

Hence we investigated the spring constant as a function of penetrator inclination for both the horizontal and vertical components under both Earth's and lunar environments (temperature and gravity). Fig. 8 shows the schematic diagram of the two sensor components sustained by the silicone components (a pair of friction wheels and the base of bearings) in the gimbal mechanism under Earth's and lunar gravity, and sensors are set at neutral positions. The silicone components are expressed as the springs by analogy in the figure. The effects of the silicone



**Fig. 9.** Schematic diagram of the horizontal sensor sustained by the horizontal friction wheel. This figure also indicates the cross-sectional view of the gimbal mechanism from the tail (or the head) side as shown in Fig. 3. The horizontal friction wheel is firmly attached to the external cylinder of the gimbal mechanism by the frictional force and sustains the attitude of the horizontal sensor.

components will differ with each sensor component, related to its contact positions.

Though the movement of the sensor to horizontal direction is restricted by the bearings, a minute clearance between the gimbal blocks and the bearings are held for rotation of the gimbal mechanism. The horizontal friction wheel sustains the gimbal blocks to compensate the clearance. The friction wheels have much lower spring constants than that of the radial direction of the bearings. For the reason, we can say that only the horizontal friction wheel can act as a spring in the oscillating direction of the horizontal sensor pendulum set in the neutral position (Fig. 8). Fig. 9 shows the schematic diagram of the horizontal sensor supported by the horizontal friction wheel. Here, we derive the spring constant of the horizontal friction wheel as a function of the penetrator inclination in both Earth's and lunar environments using the following equations:

$$K_e(T_e) = F_e(T_e)/U_e(T_e),$$

$$F_e(T_e) = F_0(T_e) + Mg_e \sin(2\pi\theta_p) \cos(2\pi\theta_r), \quad (9)$$

$$K_m(T_m) = F_m(T_m)/U_m(T_m),$$

$$F_m(T_m) = F_0(T_m) + Mg_m \sin(2\pi\theta_p) \cos(2\pi\theta_r), \quad (10)$$

where  $K$  is the spring constant in N/m,  $F$  is the vertical load of the gimbal mechanism on the horizontal friction wheel in N,  $U$  is the shrinkage of the horizontal friction wheel in m,  $g$  is the gravitational acceleration in  $m/s^2$ , and the subscripts “e” and “m” indicate the values in the Earth's and lunar environments, respectively. In addition,  $M$  is the mass of the gimbal mechanism block in kg,  $\theta_p$  is the inclination of the penetrator from the vertical in degrees (Fig. 8), and  $\theta_r$  is the angle between the line  $X$  in Fig. 9 and the contact point of the horizontal friction wheel with the external cylinder of the gimbal mechanism in the cross-sectional surface perpendicular to the longitudinal axis of the penetrator.  $T_e$  is room temperature on the Earth:  $+20^\circ\text{C}$  and  $T_m$  is the temperature in the lunar regolith near the lunar equator:  $-20^\circ\text{C}$ .  $U_e(T_e)$  and  $U_m(T_m)$  are derived from measurements shown in Fig. 7 using values of  $F_e(T_e)$ , and  $F_m(T_m)$ . The value of  $F_0$  indicates that an initial force required to support the sensor without gravitational load of the gimbal mechanism (i.e.,  $\theta_p = 0^\circ$ ). Fig. 10 shows the calculated spring constant of the horizontal friction wheel as a function of inclination of the penetrator under both Earth's and lunar conditions, using Eqs. (9) and (10). The results indicate that the spring constant is larger for the horizontal sensor on the Moon compared to the Earth regardless of the penetrator inclination.

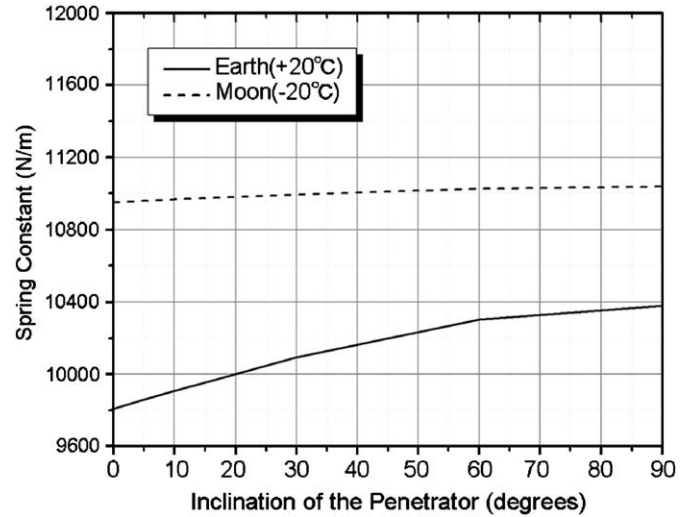


**Fig. 10.** The relationship between the inclination of the penetrator and the spring constants of the horizontal friction wheel on the Earth ( $+20^\circ\text{C}$ ) and the Moon ( $-20^\circ\text{C}$ ). These values are derived on the assumption that all weights of the gimbal mechanism load on only the horizontal friction wheel.

For the vertical component, when the penetrator is deployed with its longitudinal axis parallel to the sensitive axis of the vertical sensor whose pendulum is set in a neutral position, the base of the bearings can act as a spring in the oscillating direction of the vertical pendulum because it mostly shrinks to only axial direction. Although the spring constant of the base of the bearings does not change due to the load of the gimbal mechanism because of its linear shrinkage, its spring constant can increase due to hardening of the silicon rubber cap under the lunar low temperatures.

The vertical friction wheel can also act as a spring to the vertical sensor pendulum set in a neutral position. The neutral position of the vertical sensor pendulum is designed to be met at  $0^\circ$  from the vertical under the lunar gravity and at  $80^\circ$  from the vertical under the Earth's gravity. For this reason, we simulated the spring constant of the vertical friction wheel at  $0^\circ$  inclination from the vertical in the lunar environment, and the spring constant at  $80^\circ$  inclination from the vertical in the Earth environment. As was the case for the horizontal component, the calculated result showed that the vertical component had the spring constant is larger on the Moon compared to the Earth's. Tighter coupling of the vertical sensor, as well as the horizontal sensor, with the penetrator can be achieved on the Moon compared to the Earth. If the PSS has the proper response to ground motion after penetration under the Earth's condition, it will be preserved on the Moon.

### 3.3. Effect on the noise level

The input equivalent noise of the PSS changes with temperature. From Eq. (3), the thermal noise is reduced by decrease in temperature ( $T$ ), then, the decrease in coil resistance ( $R_C$ ) under low temperature also reduces the noise. The coil resistance will decrease by about 25% from  $+20$  to  $-20^\circ\text{C}$ .

The suspension noise will change following to Eqs. (4) and (5). Using the temperature dependence of the frequency response derived in Section 3.1, we can estimate the value of the suspension noise of the PSS at  $-20^\circ\text{C}$ . The voltage PSD of the input equivalent noise of the PSS at  $-20^\circ\text{C}$  is also shown in Fig. 5.

#### 4. Effects of the penetrating impact

After penetration into the lunar regolith, the PSS should maintain the frequency response, response to ground motion, and noise level to detect lunar seismic events. An impact test was conducted using a penetrator containing the seismometer system. The fully integrated penetrator was fired into a target of lunar simulat at a velocity of about 330 m/s, at an attack angle of 8.6°, using the Davis gun at the Sandia National Laboratory in New Mexico. This impact condition was designed to be severer than expected on the Moon (Mizutani et al., 2000). Predicted and simulated impact conditions are compared in Table 2. If the PSS can preserve the performance required to observe lunar seismic events after the impact test, we predict that the system can function well after the actual impact into lunar regolith.

##### 4.1. Frequency response after the penetration

The frequency response of the PSS after the simulated impact can be evaluated from analysis of calibration pulses sent through the total system (the PSS assembled into the penetrator).

We set the penetrator in a very quiet place where micro-tremors (seismological noise) were very low, to obtain clear calibration pulses and determine the frequency response precisely. We selected a tunnel at the Inuyama Seismic Observatory of Nagoya University (hereafter INU) in Central Japan as the quiet place. Fig. 11 compares a calibration pulse obtained from one trial in our laboratory with that at the INU. As shown in the records

**Table 2**

Comparison between the predicted impact condition on the lunar surface (Mizutani et al., 2000) and the simulated impact performed at the Sandia National Laboratory (SNL)

	Predicted impact on the lunar surface	Simulated impact at SNL
Impact acceleration	About 8000 (G)	About 10,000 (G)
Impact velocity	285 (m/s)	330 (m/s)
Attack angle	8.6° (maximum)	8.6°

after 1.0 s in Fig. 11, although the calibration pulse obtained in our laboratory is disturbed by the seismic noise whose amplitudes are about 100–200 DU, the pulse in INU is almost not disturbed by the seismic noise. The seismological noise level at the INU is lower by two orders of magnitude than that in our laboratory.

The resonant frequency, the damping constant, and the total gain of the two sensor components derived from the calibration pulses are listed in Table 3. We assume that the generator constants of the two sensors and the amplifier gain of the electronics hardly changed after the penetration. The frequency response of the system after the impact is estimated from the parameters listed in Table 3 and Eq. (1).

##### 4.2. Response to ground motion after the penetration

The response of the sensor itself to ground motion after the simulated impact has been already confirmed to be accurate from comparison with the response of the Streckeisen STS-2 (a high performance, portable, very broadband tri-axial seismometer) (Yamada et al., 2005).

To verify the response of the entire assembled PSS to ground motion after the penetration, we carried out a second seismic observation test. In this test, seismic waveforms recorded by the both PSS and two types of reference seismometers were compared. One of the reference sensors was identical to those inside the PSS, only not assembled into a penetrator. The identical pre-amplifier to that of PSS was attached with the reference sensor. The other reference sensor was an L-4C

**Table 3**

The resonant frequencies, damping constants, and total gains of the two sensor components of the penetrator seismometer system, after penetration

	Horizontal	Vertical
Resonant frequency (Hz)	$1.387 \pm 0.014$	$1.466 \pm 0.017$
Damping constant	$0.578 \pm 0.010$	$0.558 \pm 0.010$
Total gain (generator constant*amplifier gain)	$1050 * 6000$	$1050 * 6000$

Resonant frequency and damping constant are values measured at +18 °C in the tunnel at INU.

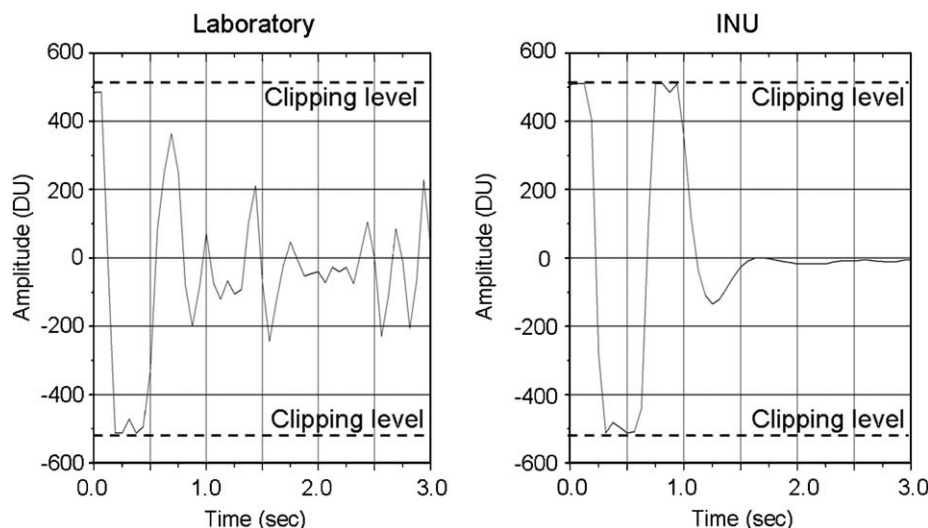


**Fig. 11.** The calibration pulses of the PSS obtained from one trial in our laboratory (left figure) and in the Inuyama Seismic Observatory of Nagoya University (INU) (right figure). The 0 s mark on the time axis indicates the beginning of the record of the calibration pulse. The pulse data before 1.0 s is clipped over the dynamic range of the PSS. The data after 1.0 s are used as the calibration pulse for the analysis.

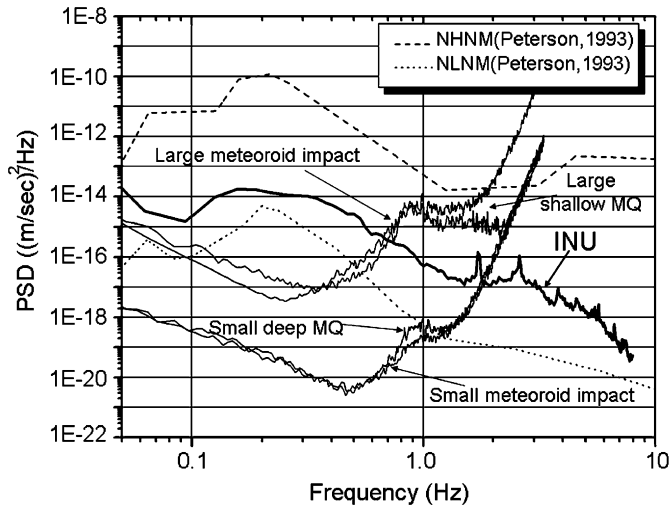


**Fig. 12.** The averaged PSD of microtremors at INU and those of some types of lunar seismic events: a large meteoroid impact (71\_163\_1051\_Y), a large shallow moonquake (75\_003\_0147\_X), a small deep moonquake (72\_160\_1619\_X), and a small meteoroid impact (71\_211\_0920\_Y). These lunar seismic events were detected by the Apollo 14 LP seismometer, and their PSD profiles were corrected for the frequency response of the Apollo LP instrument in peaked response mode. These PSD profiles are compared with the New High Noise Model (NHHM) and the New Low Noise Model (NLNM) (adapted from Peterson, 1993).

geophone (a short-period electromagnetic seismic sensor produced by the former Mark Products) with a resonant frequency of 1 Hz.

In the observation test, we focused on the response to faint ground motions (microtremors), because moonquakes are known to be very small, with magnitudes of about 0.5–1.3 on the Richter scale (Lammlin, 1977), and many events have the maximum velocity amplitudes of about 1.0–2.0 E-9 m/s at 1 Hz. The microtremors at the INU are also small; the average level of their velocity amplitudes is in the range of 5E-9–1E-8 m/s at 1 Hz. In Fig. 12, the averaged PSD of the microtremors at the INU is compared with PSD profiles of some types of lunar seismic events, as well as the New High-Noise Model (NHHM) and the New Low-Noise Model (NLNM), adapted from Peterson (1993). Though the microtremors at the INU are larger than typical lunar seismic motions, we made the observation test at the INU as best as we could.

In the tunnel at the INU, the penetrator was set at an inclined angle of about 80° from the vertical. As described in Section 3.2, at this inclination, the effect of elasticity of the gimbal mechanism on the response of two sensor components is largest. If the proper response of the seismometer system to ground motion is achieved at the inclined angle, the waveforms observed on the Moon will not be influenced by the elastic contacts. The photograph of the penetrator set in the tunnel is shown in Fig. 13.

After the deployment of the penetrator, the attitudes of the two-component sensors in the penetrator were adjusted by the gimbal mechanism. Then the seismic observation was made by three types of seismometers: the PSS and the two types of reference sensors set in close proximity to one another.

At one trial of the test, microtremors were observed for 1024 s. Since the recording conditions and frequency response of the PSS are different from those of the reference sensors which have a resolution of 24 bits, and a sampling rate of 200 Hz, each data observed by references and PSS was corrected so that they could be compared with each other. In the correction for PSS data, the frequency responses of the two sensor components of the PSS were corrected using values listed in Table 3.

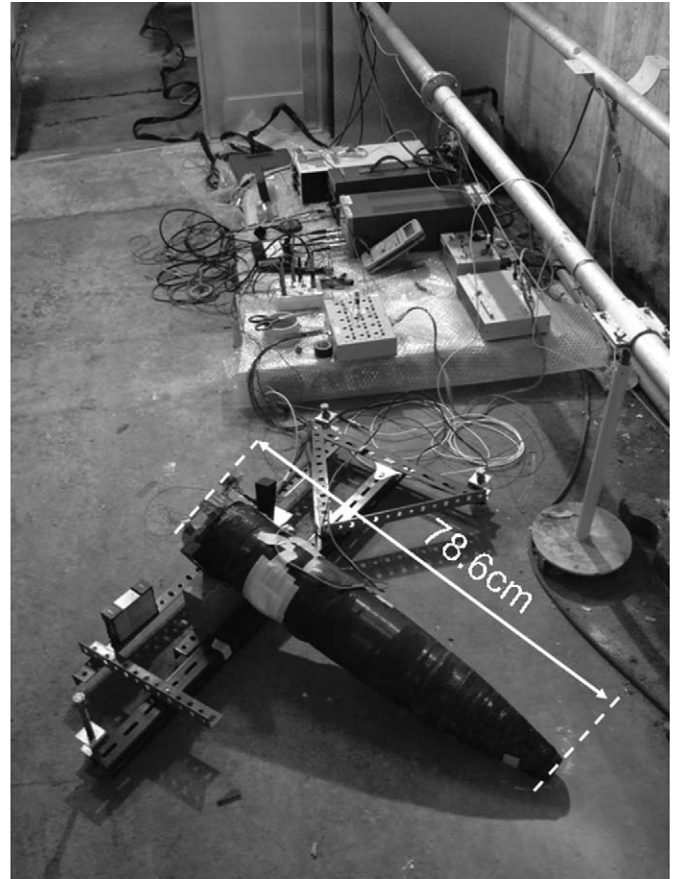


**Fig. 13.** Photograph of the qualification model of penetrator set in the tunnel at INU. An external power supply, a current probe for monitoring the penetrator operation, and a wired-cable of antenna for communication are also set near by the qualification model.

Examples of corrected waveforms for the horizontal and vertical sensors over a period of 50 s are plotted in Fig. 14. These waveforms were filtered by a band pass filter between 0.50 and 6.00 Hz to emphasize this frequency range. The correlation coefficients in time series between the data observed by the reference sensors and that by the PSS were calculated, and were larger than 0.90 in these frequency ranges on both the horizontal and vertical components.

In order to compare the observed waveforms in the frequency domain, we calculated the PSD as follows: we divided a time series of the observed ground motion into 64 segments of 32 s in length. Successive segments overlapped each other by 16 s. We removed the mean and linear trend from each segment and calculated the discrete Fourier components  $X_i(f)$  of each segment using a Hanning window, where the subscript  $i$  indicates the  $i$ th segment. Then, the PSD of the time series was calculated by

$$\text{PSD}(f) = (1/N) \sum_{i=1}^N (X_i(f)X_i^*(f))/T, \quad (11)$$

where  $N$  is the total number of segments (64),  $T$  is the time length: (32 s), and  $X_i^*(f)$  is the conjugated component of  $X_i(f)$ . Fig. 15(a) and (b) show the PSD profiles of the corrected waveforms observed by the horizontal and vertical sensors, respectively.

Figs. 14 and 15 indicate that there are good similarities among the observed waveforms. The response of the PSS to ground motion after penetration agrees well with the responses of the reference sensors.

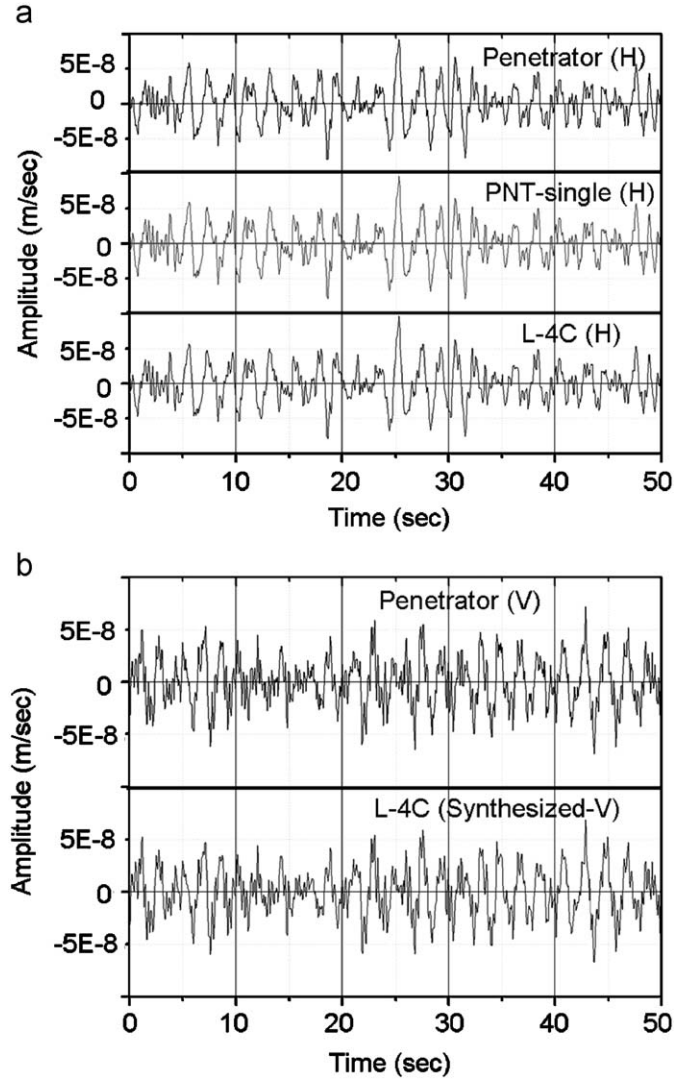


**Fig. 14.** Corrected waveforms as observed by the PSS and two reference seismometers on (a) the horizontal (H) and (b) the vertical (V) components. These waveforms are filtered between 0.50 and 6.00 Hz. The abbreviation 'PNT-single' means our single sensor not assembled into the penetrator. The waveform observed by the vertical sensor in the PSS is compared with a synthesized component of L-4C, since our vertical sensor is set at about  $10^\circ$  inclination from the horizontal. The 'Synthesized' waveform is derived from summing (cosine of about  $10^\circ$ ) horizontal component + (sine of about  $10^\circ$ ) vertical component, as observed by the L-4C sensors.

#### 4.3. Noise level after the penetration

To estimate the noise level of the PSS after the impact test, we calculated the coherence among microtremors observed by the three types of seismometers. The coherence function can be used to provide preliminary estimates of the system's signal-to-noise ratio (Holcomb, 1989). The coherence is expressed as

$$\text{coh}^2(f) = |P_{12}(f)|^2 / (P_1(f)P_2(f)), \quad (12)$$

where  $\text{coh}^2$  is the square of the coherence, and  $P_1$  and  $P_2$  are the power spectral densities of seismic data observed by sensor 1 and sensor 2, respectively, calculated in the same manner as in Eq. (11).  $P_{12}$  is the cross spectral density (CSD) between the data observed by sensor 1 and sensor 2; it is expressed as

$$\text{CSD}(f) = (1/N) \sum_{i=1}^N (X_i(f)Y_i^*(f))/T, \quad (13)$$

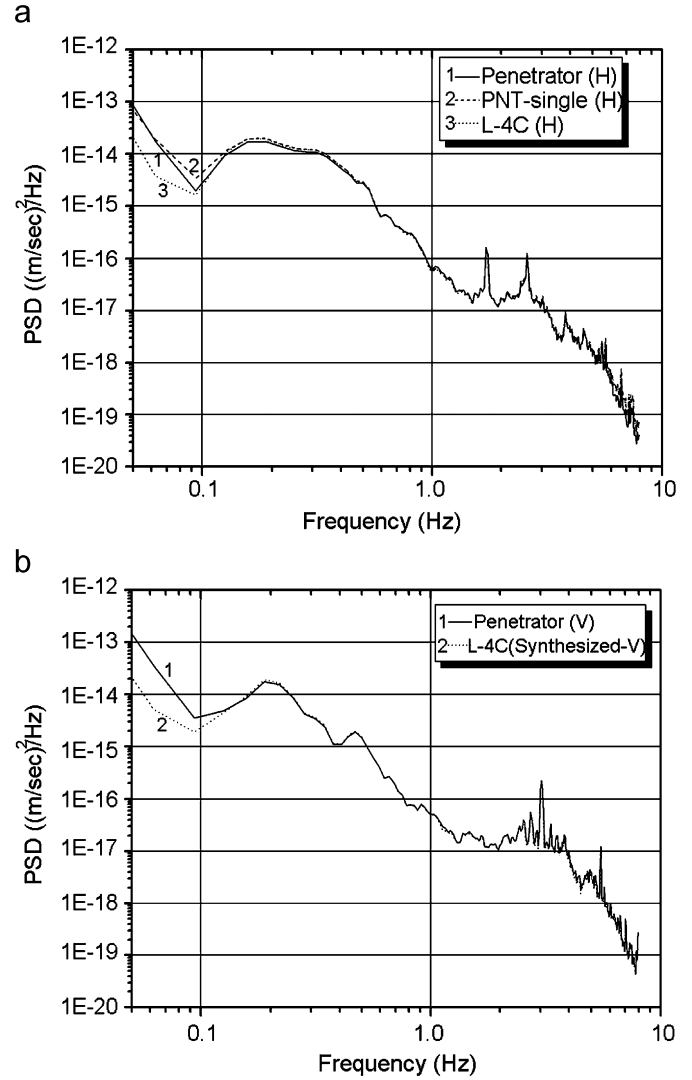


**Fig. 15.** The averaged PSD profiles calculated from waveforms observed by the PSS and two reference seismometers on (a) the horizontal (H) and (b) the vertical (V) components. The description of 'Synthesized' is the same as the caption of Fig. 14.

where  $X_i(f)$  is the  $i$ th discrete Fourier component of the segmented signal observed by sensor 1 and  $Y_i(f)$  is that observed by sensor 2,  $N$  is the total number of segments (64), and  $T$  is the time length (32 s), as in the calculation of the PSD.

The degree of incoherency among seismometers represents the noise of each instrument. If the PSS can observe a microtremor as well as the reference sensors, the square of the coherence will be approximately 1.0, indicating that there is little contamination by instrumental noise.

Fig. 16(a) and (b) show the coherence between any two instruments for the horizontal and vertical sensor components, respectively. The coherence is typically close to 1.0 in the frequency range 0.2–6.0 Hz. These results show that the PSS performs well, for the observation of microtremors. Since the input equivalent noise at the input stage of the pre-amplifiers of the PSS and that of the single sensor not assembled into the penetrator (reference sensor) are very similar, we conclude that the noise level of the PSS does not change after penetration. In addition, since the gimbal mechanism is composed of the material which has strength enough to resist against the impacting shock and its interior is sealed tightly, we assumed that xenon gas did not leak out from the gimbal mechanism by the

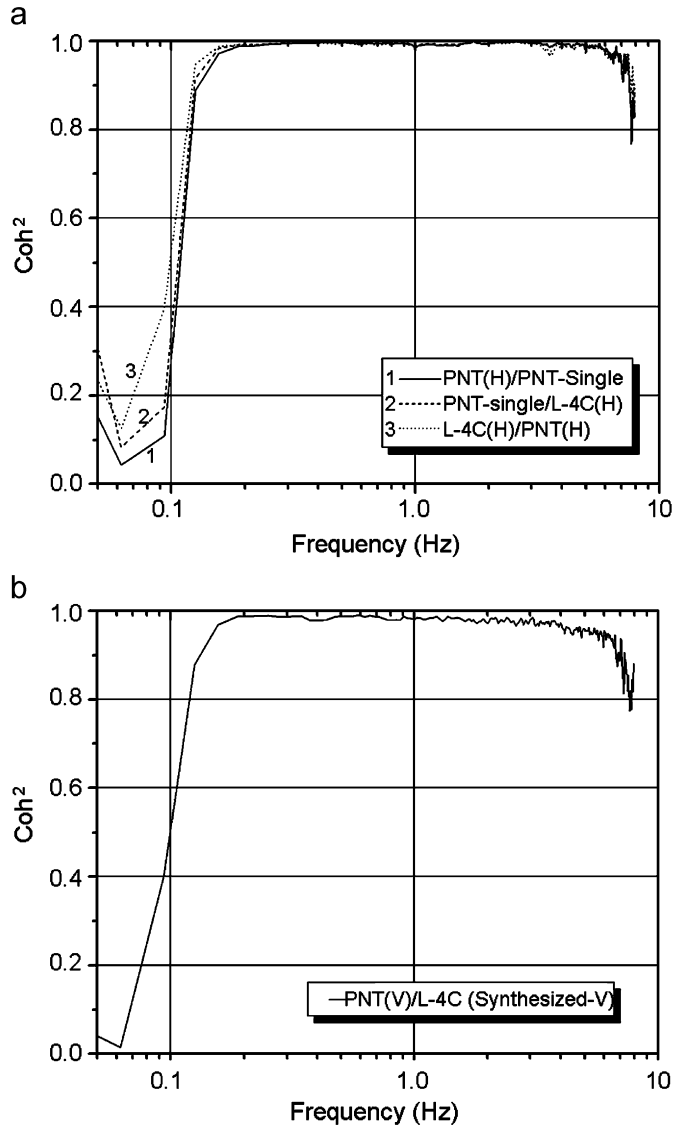


**Fig. 16.** The averaged coherence calculated from waveforms observed by the PSS and two reference seismometers on (a) the horizontal (H) and (b) the vertical (V) components. The description of ‘Synthesized’ is the same as the caption of Fig. 14.

impact, so suspension noise is expected. We can apply the voltage PSD model described in Section 2.3 to represent the noise level after penetration.

### 5. Detection capability of the PSS on the moon

Taking all of our test results into account, we evaluated the capability of the PSS for seismic event detection on the lunar surface. The values relevant to the frequency response listed in Table 3 report the characteristics of the seismometer system after the penetration. However, these will change due to the low temperature (about  $-20^{\circ}\text{C}$ ) at  $\sim 2\text{ m}$  depth in the lunar regolith. The predicted values in the lunar regolith can be estimated using the correction coefficients for temperature described in Section 3.1. We apply these coefficients to the frequency response of two sensor components. Table 4 shows the corrected values for two sensor components. We assume that these values correspond to those predicted in the lunar regolith after penetration, although they could be taken as a worst case scenario since our tests

**Table 4**

The characteristics of two sensor components of the penetrator seismometer system which are assumed to be achieved in the lunar regolith near the lunar equator, after penetration

	Horizontal	Vertical
Resonant frequency (Hz)	$1.235 \pm 0.014$	$1.413 \pm 0.014$
Damping constant	$0.669 \pm 0.010$	$0.589 \pm 0.010$
Total gain (generator constant*amplifier gain) (V/m/s)	$1065 * 6000$	$1065 * 6000$

employed a higher impact shock than predicted on the lunar surface as shown in Table 2.

In Fig. 4, a comparison of the frequency response curve of the PSS (horizontal) using the parameters listed in Table 4 with those of the Apollo seismometers is also shown. This figure shows that the PSS can preserve a higher gain in the higher frequency range over 1 Hz than those of the Apollo seismometers even after a hard landing on the Moon.

The input equivalent noise of the PSS after deployment in the lunar regolith can be represented using Eqs. (3)–(7) and the parameters listed in Table 4, as described in Sections 3.3 and 4.3. Since we have to examine whether our short-period seismometer system can detect deep moonquakes with small amplitudes as described in Section 2.1, we evaluate the signal-to-noise ratio for small deep moonquakes. We define a small deep moonquake as an event whose amplitude is comparable to about the least significant amplitude measurable by the Apollo digital recording system, which is about  $1.5\text{E-}9\text{ m/s}$  in terms of velocity at 1 Hz. We selected events that were identified as deep moonquake signals in other papers (Nakamura et al., 1981; Lognonné et al., 2003). The moonquake data were corrected for the frequency response of the Apollo seismometers, and the frequency response of the PSS using parameters of the horizontal sensor listed in Table 4 was convolved with the corrected data. If a converted small deep moonquake signal has larger amplitudes than that of the noise of the PSS, that is, the signal-to-noise ratio is larger than 1, the event can be detected.

To confirm the small moonquake detection capability, we converted the noise model from the frequency domain to the time domain. We synthesized a waveform that represented the noise model at  $-20^{\circ}\text{C}$  as shown in Fig. 5 using uniform random numbers. In the frequency domain, the waveform was synthesized to have the identical voltage PSD to the noise model. The convolved noise waveform was converted from voltage to velocity units using the value of the generator constant in Table 4, and filtered between 0.01 and 6.00 Hz, designed values in the measurement electronics (Table 1). Then, the synthesized waveform of the noise component was derived, and had maximum amplitude of about  $1.2\text{E-}9\text{ m/s}$ .

For small deep moonquake events, the signals of three components (two horizontal: X, Y, and one vertical: Z) were compared with the noise waveform of the PSS. As an example, in Fig. 17, we show a comparison of a deep moonquake (72\_160\_1619\_Y) observed at Apollo 14 with the noise waveform. The notation (72\_160\_1619\_Y) indicates that the event occurred at 16:19, 160 days, and 1972, and it was detected by the horizontal component (Y) of Apollo LP. Fig. 17(a) indicates the original data observed by Apollo LP seismometer, and Fig. 17(b) indicates the calculated waveform assumed to be observed by the PSS, together with the estimated noise waveform. In Fig. 17(b), the larger amplitude of the event than that of the noise indicates the signal-to-noise ratios is over 1. This is also the case for the remaining components (X, Z).

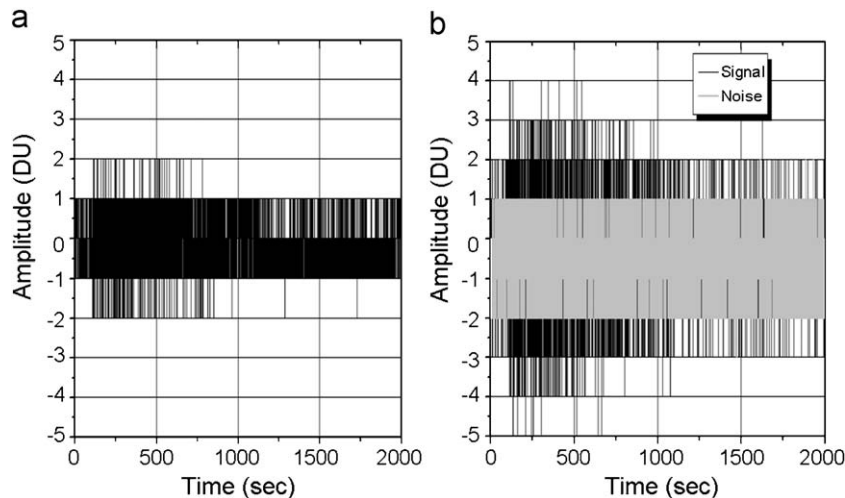


**Fig. 17.** (a) A deep moonquake event (72\_160\_1619\_Y) as observed by the horizontal component (Y) of the Apollo 14 LP instrument and (b) that assumed to be detected by the horizontal sensor of the PSS in the lunar regolith. The 0 s mark indicates the arrival time of the P-wave (Lognonné et al., 2003). The noise waveform of the PSS is compared with the signal in figure (b). Recording of the waveforms with a sampling rate of 16 Hz and a dynamic range of 10 bits are simulated for the PSS.

It is considered that the frequency content of lunar seismic events are different for each Apollo station, and that this may be caused by differences in local regolith thickness and structure (Latham et al., 1973; Nakamura et al., 1975; Horvath et al., 1980). For this reason, we investigated small deep moonquake events recorded at other sites (Apollo 12, 15, and 16 sites) and found that the small deep moonquakes recorded at all of the Apollo sites can be detected by our seismometer system.

From these results, we conclude that seismic events with amplitudes larger than 1 DU as recorded by Apollo will be able to be detected by our seismometer system. In addition, Fig. 17 shows that the PSS can record the small deep moonquakes with larger amplitude than the Apollo recordings. The same conclusion is also shown for the vertical sensor of the PSS.

## 6. Conclusion

We have confirmed that the PSS can preserve the sensitivity required to detect small deep moonquakes as well as other types of lunar seismic events and have the proper response to small ground motions in the lunar environment, after a harder penetration than that predicted into the lunar regolith. By taking advantages of the unique qualities of our penetrator, we can deploy multiple seismic stations, providing an ideal setup for seismic observations. We hope that the seismometer system will be deployed on the Moon and that will successfully obtain new lunar seismic data. This data will enable a better understanding internal structure of the Moon, including the core.

## Acknowledgement

We thank Dr. Yasuhiro Yokota for his technical support in the entire study and some colleagues for their assistance in the observation test at the seismic observatory. Technical staffs at the IHI Aerospace Co., Ltd. are greatly acknowledged for their dedicated work during the development of penetrator seismometer system. We would like to express special thanks to Renee Weber for constructive review and Axel Hagermann for editorial suggestion that helps to improve the manuscript.

## References

- Aki, K., Richards, P.G., 2002. Principles of seismology. In: Quantitative Seismology, Second ed. University Science Books, pp. 595–645.
- Araki, H., 1994. The clarification of the moonquake occurrence mechanism and the application of it to LUNAR-A mission. Ph.D. Thesis of the University of Tokyo (in Japanese).
- Chikazumi, S., 1981. The various magnetism. In: Physics of Ferromagnetism, Magnetic Properties of Matter, Vol. 1. Publishing Inc., Shokabo, pp. 124–132 (in Japanese).
- Dainty, M.A., Goins, R.N., Toksöz, N.M., 1975. Natural lunar seismic events and the structure of the moon. In: Proceeding of Lunar and Planetary Science Conference sixth, pp. 2887–2897.
- Gagnepain-Beyneix, J.G., Lognonné, P., Chenet, H., Lombardi, D., Spohn, T., 2006. A seismic model of the lunar mantle and constraints on temperature and mineralogy. *Physics of the Earth and Planetary Interiors* 159, 140–166.
- Goins, R.N., Toksöz, N.M., Dainty, M.A., 1979. The lunar interior: a summary report. In: Proceeding of Lunar and Planetary Science Conference 10th, pp. 2421–2439.
- Goins, R.N., Dainty, M.A., Toksöz, N.M., 1981. Seismic energy release of the moon. *Journal of Geophysical Research* 86 (B1), 378–388.
- Havskov, J., Alguacil, G., 2004. Seismic sensors. In: Instrumentation in Earthquake Seismology. Springer, Berlin, pp. 11–76.
- Holcomb, G.L., 1989. A direct method for calculating instrument noise levels in side-by-side seismometer evaluations. Open-File-Report 89-214. US Department of Interior Geological Survey.
- Horvath, P., 1979. Analysis of lunar seismic signals—determination of instrument parameters and seismic velocity distributions. Ph.D. Thesis of University of Texas at Dallas.
- Horvath, P., Latham, V.G., Nakamura, Y., Dorman, J.H., 1980. Lunar near-surface shear wave velocities at the Apollo landing sites as inferred from spectral amplitude ratios. *Journal of Geophysical Research* 85 (B11), 6572–6578.
- Khan, A., Mosegaard, K., 2002. An inquiry into the lunar interior: a nonlinear inversion of the Apollo lunar seismic data. *Journal of Geophysical Research* 107 (E6), 1–18.
- Lammlein, D., 1977. Lunar seismicity and tectonics. *Physics of the Earth and Planetary Interiors* 14, 224–273.
- Lammlein, R.D., Latham, V.G., Dorman, J., Nakamura, Y., Ewing, M., 1974. Lunar seismicity, structure, and tectonics. *Reviews of Geophysics and Space Physics* 12 (1), 1–21.
- Langseth, M.G., Keihm, S.J., 1977. In-situ measurements of lunar heat flow. Soviet-American Conference on Geochemistry of the Moon and Planets NASA SP-370, pp. 283–293.
- Latham, G., Ewing, M., Press, F., Sutton, G., Dorman, J., 1970. Passive Seismic Experiment. Apollo 12 Preliminary Science Report, pp. 39–53.
- Latham, G., Ewing, M., Dorman, J., 1973. Lunar structure and dynamics—results from the Apollo passive seismic experiment. *The Moon* 7, 396–420.
- Lognonné, P., Gagnepain-Beyneix, J.G., Chenet, H., 2003. A new seismic model of the moon: implication for structure, thermal evolution and formation of the moon. *Earth and Planetary Science Letters* 211, 27–44.

- Mizutani, H., Fujimura, A., Hayakawa, M., Tanaka, S., Shiraishi, H., 1999. LUNAR-A penetrator: its science and instruments. In: Kömle, N.J., Kargl, G., Ball, A.J., Lorenz, R.D. (Eds.), *Penetrometry in the Solar System*. Austrian Academy of Sciences Press, Vienna, pp. 125–136.
- Mizutani, H., Fujimura, A., Hayakawa, M., Tanaka, S., Shiraishi, H., Yoshida, S., 2000. LUNAR-A MISSION: science objectives and instruments. In: *ICEUM-4 Proceeding of Fourth International Conference on the Exploration and Utilization of the Moon*, pp. 107–114.
- Mizutani, H., Fujimura, A., Tanaka, S., Shiraishi, H., Nakajima, T., 2003. LUNAR-A MISSION: goals and status. *Advances in Space Research* 31, 2315–2321.
- Nakamura, Y., Dorman, H.J., Duennebier, F., Lammlein, D., Latham, G., 1975. Shallow lunar structure determined from the passive seismic structure. *The Moon* 13, 57–66.
- Nakamura, Y., Latham, V.G., Dorman, J.H., Harris, E.J., 1981. Passive seismic experiment long-period event catalog. Technical Report 118, Rev. ed., University of Tex. Inst. for Geophysics., Austin.
- Nakamura, Y., Latham, V.G., Dorman, H.J., 1982. Apollo lunar seismic experiment-final summary. *Journal of Geophysical Research* 87 (Supplement), A117–A123.
- Peterson, J., 1993. Observations and modeling of seismic background noise. Open-File Report 93-322. US Department of Interior Geological Survey.
- Rodgers, W.P., 1992. Frequency limits for seismometers as determined from signal to noise ratios. Part.1. the electromagnetic seismometer. *Bulletin of the Seismological Society of America* 82 (2), 1071–1098.
- Shiraishi, H., Tanaka, S., Fujimura, A., Hayakawa, H., 2008. The present status of the Japanese penetrator mission: LUNAR-A. *Advances in Space Research* 42, 386–393.
- Toksöz, N.M., Dainty, M.A., Solomon, C.S., Anderson, R.K., 1974. Structure of the Moon. *Reviews of Geophysics and Space Physics* 12 (4), 539–565.
- Yamada, R., Yamada, I., Yokota, Y., Shiraishi, H., Tanaka, S., Fujimura, A., Mizutani, H., Kobayashi, N., Takeuchi, N., Murakami, H., Ishihara, Y., Koyama, J., Yomogida, K., Takagi, Y., 2005. Seismometer design and its characteristics onboard LUNAR-A penetrator. In: *Proceedings of 6th IAA International Conference on Low-Cost Planetary Missions*, pp. 433–440.